Supplementary Information for Parallel Wavelength-Division-Multiplexed Signal Transmission and Dispersion Compensation Enabled by Soliton Microcombs and Microrings

Supplementary Note 1: Program-controlled scheme for the single-soliton generation and stabilization

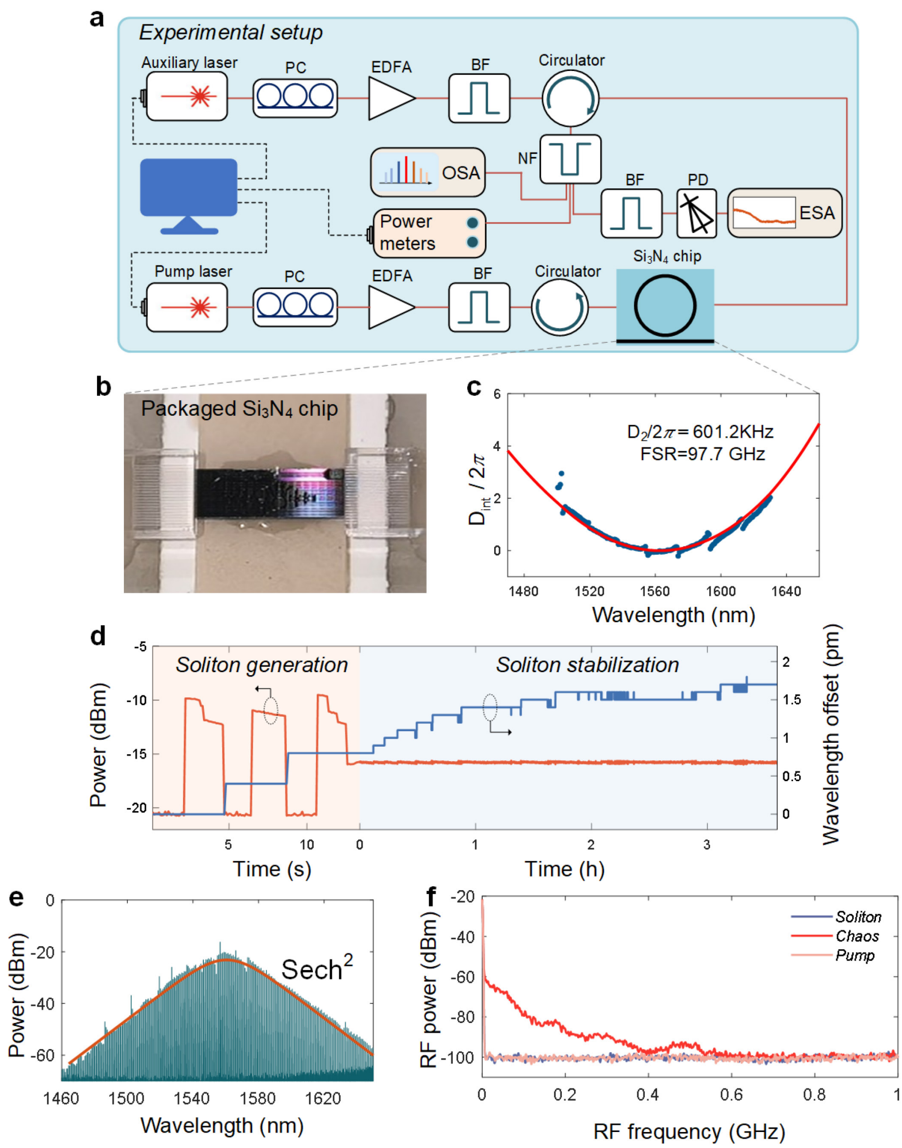

Supplementary Fig. 1. Program-controlled single-soliton microcomb generation and stabilization. a Experimental setup for the single-soliton generation and stabilization. PC: polarization controller; EDFA: erbium-doped fiber amplifier; BF: bandpass filter; NF: notch filter; OSA: optical spectrum analyzer; ESA: electric spectrum analyzer; PD: photodetector. **b** Photograph of the packaged Si_3N_4 chip. **c** Integrated dispersion of the adopted TE_0 mode. The $D_2/2\pi$ is 601.2 kHz and the FSR is 97.7 GHz. **d** Comb power and auxiliary laser wavelength variation traces during the single-soliton generation and stabilization process. We monitor a small portion of the comb power through the 1:9 splitter. **e** Spectrum of the single soliton with a smooth sech^2 envelope. **f** RF spectrum at low RF frequency when we filter out the single line to the PD of the single soliton, chaos combs, and pump laser.

We implemented a program-controlled scheme based on the red-detuned pump entrance forward-tuning method with the assistance of an auxiliary laser to generate the long-term single-soliton microcomb[1]. The thermal lock effect of the auxiliary laser on the blue-detuned side can ensure the pump laser to approach the soliton state. The schematic experimental setup is shown in Supplementary Fig. 1a. Two counter-propagating optical waves from the pump and from the auxiliary lasers were coupled into the silicon nitride (Si_3N_4) microresonator. We utilized an optical circulator to separate the pump light and the auxiliary light. Meanwhile, we utilized a notch filter to filter out the pump light and the reflective auxiliary light. Then, we recorded the optical spectra during the comb evolution with an optical spectrum analyzer (OSA) and characterized the low-frequency noise property by using an electrical spectrum analyzer (ESA). We measured the comb power during the tuning process to determine the generation of the single soliton. The output powers of the pump and of the auxiliary laser were set to 31 dBm and 32 dBm and the coupling loss is ~3 dB/facet after the packaging, as shown in Supplementary Fig. 1b. Supplementary Figure 1c depicts the integrated dispersion curve of the adopted TE_0 mode. The TE_0 mode has an anomalous dispersion[2] with the $D_2/2\pi$ of 601.2 kHz and a free spectral range (FSR) of 97.7 GHz. The single soliton can be generated with a high probability only when the auxiliary laser supports an efficient thermal compensation[1].

We adopted the iteration method to generate the single soliton and the tuning process is shown in Supplementary Fig. 1d. These two traces represent the variations of the comb power and of the wavelength offset of the auxiliary laser during the generation and the stabilization process. During the soliton generation, we performed the forward scanning with the red-detuned entrance for the pump laser, and the auxiliary laser wavelength was fixed during the pump tuning process. If a single soliton is not generated, the auxiliary laser wavelength is increased by 0.4 pm, and the pump scanning process restarts. After several iterations, we can deterministically generate the single soliton, and we begin the stabilization procedure. The pump laser wavelength was fixed during the soliton stabilization process. We tuned the auxiliary laser wavelength to vary the intracavity power of the auxiliary laser, and the position of the pump resonance changed accordingly due to the thermal effect and to the cross-phase modulation (XPM) of the auxiliary laser under a high power. Therefore, we precisely tuned the auxiliary laser wavelength to lock the comb power to the value when the single soliton was initially generated. In the experiment, the single soliton was stabilized for more than 3 hours. Supplementary Figure 1e shows the recorded spectrum of the single soliton with a smooth $sech^2$ envelope. Compared to the chaotic comb, the single soliton has a lower noise which is similar to that of the pump laser, as shown in Supplementary Fig. 1f.

Supplementary Note 2: Simulations of the reconfigurable MRRs-based dispersion compensator

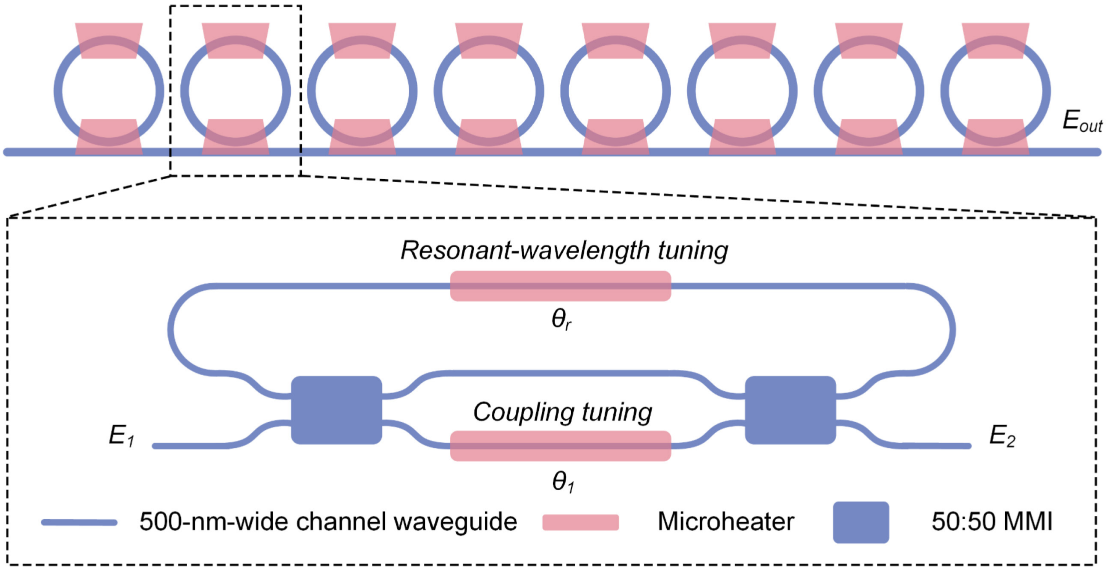

Supplementary Fig. 2. Schematic structure of the dispersion compensator. Inset: Enlarged schematic structure of the MRR. MMI: multimode interferometer.

We designed the dispersion compensator using the transfer matrix method. Supplementary Figure 2 shows the schematic structure of the dispersion compensator. We express the complex amplitude transmission of the i[th] coupling-tunable microring resonator (MRR) $T_{single}(i)$ as:

$$T_{single}(i) = \frac{E_2}{E_1} = je^{-j(\theta_{1_i}+\theta_{r_i})} \cdot \frac{e^{j(\frac{\theta_{1_i}}{2}+\theta_{r_i})}\sin\left(-\frac{\theta_{1_i}}{2}\right)+j\alpha_i e^{-j\phi_i}}{1+j\alpha_i e^{-j(\frac{\theta_{1_i}}{2}+\theta_{r_i})}\sin\left(-\frac{\theta_{1_i}}{2}\right)e^{-j\phi_i}} \quad (1)$$

where E_2 and E_1 are the complex amplitudes of the electric fields of the output and the input of the MRR, θ_{1_i}, θ_{r_i}, α_i, and ϕ_i represent the phase shift of the coupler, the phase shift of the i[th] MRR, the amplitude loss factor of the i[th] MRR, and the round-trip phase of the i[th] MRR. Here $\phi_i = 2\pi n_{eff} L_i/\lambda$, where n_{eff} is the effective refractive index of the waveguide in the MRR, L_i is the round-trip length of the MRR, and λ is the optical wavelength in a vacuum. All the 8 MRRs share the same design. As we utilize the Mach-Zehnder interferometer (MZI) as the tunable coupler, the equivalent power coupling coefficient of the i[th] MRR is $K_{eqv_i} = cos^2(\theta_{1_i}/2 + \Delta\phi_{ini_i})$, where $\Delta\phi_{ini_i} = \phi_{up_i} - \phi_{down_i}$ is the initial phase difference (when $\theta_{1_i} = 0$) between the two arms of the MZI, and ϕ_{up_i} and ϕ_{down_i} are the phase changes induced by the upper and the lower arms. We assume $\Delta\phi_{ini_i} = 0\ (i = 1, 2, \ldots, 8)$ in our modelling. We then model each MRR as a standard laterally coupled MRR with a real waveguide-MRR power coupling coefficient K_{eqv} (assuming no coupling loss) and with a resonator phase shift θ_r. The complex amplitude transmission of the i[th] MRR is:

$$T_{single}(i) = \frac{\sqrt{1-K_{eqv_i}}-\alpha_i e^{-j(\phi_i+\theta_{r_i})}}{1-\alpha_i\sqrt{1-K_{eqv_i}}e^{-j(\phi_i+\theta_{r_i})}} \quad (2)$$

We calculate the amplitude transmission of the eight cascaded MRRs by multiplying the amplitude transmission of each MRR as follows:

$$T_{cascaded} = \prod_{i=1}^{8} T_{single}(i) \quad (3)$$

Then, we obtain the phase and group delay responses of the cascaded MRRs as:

$$\emptyset = arctan(\frac{Im(T_{cascaded})}{Re(T_{cascaded})}) \quad (4)$$

$$\tau = -\frac{d\emptyset}{d\omega} \quad (5)$$

where $\emptyset$ is the phase response, $Im(\cdot)$ and $Re(\cdot)$ represent the imaginary and the real parts, respectively, τ is the group delay response, and ω is the optical angular frequency. We obtain the dispersion parameter D as follows:

$$D = \frac{d\tau}{d\lambda} \quad (6)$$

With the theoretical model (Eqs. (1) – (6)), we utilized a nonlinear optimization method based on the sequential quadratic programming (SQP) algorithm to optimize the real power coupling coefficient K_{eqv} and the phase shift θ_r of each MRR (K_{eqv} and θ_r are assumed independent parameters) to attain the desired dispersion compensation for different lengths of single-mode fibers (SMFs) with an operation bandwidth of 32 GHz and with a dispersion ripple of less than ±10 ps/nm. We assumed a waveguide transmission loss of 4 dB/cm in the simulations. In the simulation for 8 MRRs, we have 16 independent parameters (power coupling coefficient K_{eqv} and phase shift θ_r for each ring) to adjust to realize the target. We monitored the ripples of the calculated dispersion values within the desired bandwidth in each iteration and adjusted all the 16 independent parameters of 8 MRRs to minimize the ripples. The power coupling coefficients are constrained in the range of 0 to 1 while we impose no constraints for the phase shifts.

We set the target of the optimization to be a constant compensated dispersion value D_{tar} of the corresponding lengths of SMFs within the 32-GHz bandwidth. We define a figure-of-merit (FOM) as $FOM = 1/n \cdot \sum_{i=1}^{n}(D_i - D_{tar})^2$, where n is the number of dispersion values sampled within the bandwidth and D_i is the simulated dispersion value at a certain wavelength. For example, if we consider the bandwidth to be 0.2 nm, and the wavelength increment is 1 pm, then n is 201, D_i is the i^{th} sampled point of the simulated dispersion. The FOM reflects the variance of the dispersion within the bandwidth with respect to the target dispersion parameter. The optimization is reached when the FOM is minimized. As different numbers of MRRs are required for the dispersion compensation of various lengths of SMFs, we started from one single MRR and more MRRs were introduced one at a time. If the FOM is minimized, the number of MRRs is confirmed. If not, we add one more MRR into the optimization and implement the optimization again until we satisfied the FOM of the optimization. The optimization of the dispersion compensation for a 20-km-long SMF within a 50-GHz bandwidth is the same except for a larger preset bandwidth.

A total of 4, 5, 7, and 8 MRRs are required for dispersion compensation of the 4 lengths of SMFs in a 32-GHz bandwidth while 8 MRRs are needed for a 20-km-long SMF within a 50-GHz bandwidth. The simulated transmission and group delay responses over one FSR at the wavelength around 1558.7 nm for dispersion compensation within the 32-GHz bandwidth are shown in Supplementary Figs. 3a and 3b. The group delay varies inversely with the wavelength in the operation bandwidth while the dispersion compensation of a longer SMF exhibits a larger absolute slope. The group delay responses of each MRR and their summation for different lengths of SMFs are illustrated in Supplementary Figs. 3c to 3f. The required maximum group delays are all positive, and they are smaller for the MRRs resonant at the longer wavelength side, indicating that all the MRRs are working in the over-coupling regime and the power coupling coefficients are higher for the MRRs resonant at the longer wavelength side. Supplementary Figures 3g and 3h show the transmission

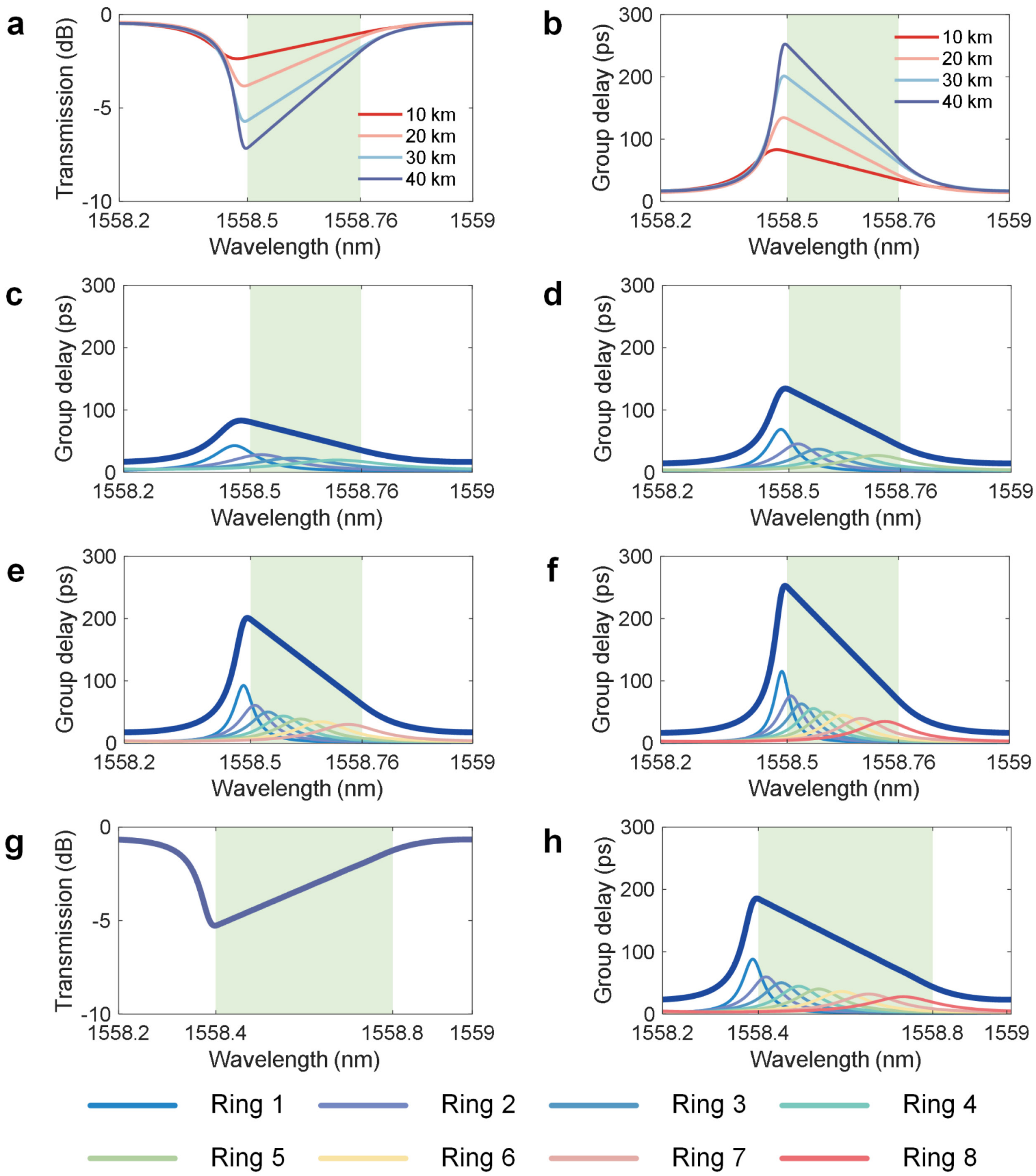

Supplementary Fig. 3. Simulations of the MRRs-based dispersion compensator. a, b Simulated **(a)** transmission spectra and **(b)** group delay responses at the wavelength around 1558.7 nm for the dispersion compensation of 10 km, 20 km, 30 km, and 40 km SMFs. **c-f** Simulated group delay responses of each MRR and their summation of dispersion compensation for **(c)** 10 km, **(d)** 20 km, **(e)** 30 km, and **(f)** 40 km SMF transmission. **g, h** Simulated **(g)** transmission and **(h)** group delay responses of dispersion compensation for 20-km-long SMF within a 50-GHz bandwidth.

and group delay responses of dispersion compensation for the 20-km-long SMF within a 50-GHz bandwidth. The simulated resonant wavelengths and group delay responses of the MRRs for dispersion compensation of the 10-, 20-, 30-, and 40-km-long SMFs in the 32-GHz bandwidth and of the 20-km-long SMF in the 50-GHz bandwidth are listed in Supplementary Table 1. The numerical data in the upper and lower rows of each grid stand for the resonance wavelength and the group delay of the corresponding MRR, respectively. The resonant wavelengths are relative to that of the first MRR. The numerical data shown in Supplementary Table 1 demonstrate that when the MRRs are tuned to the desired wavelengths with the corresponding desired group delay, we obtain a flat in-band dispersion response.

Supplementary Table 1. Simulated resonant wavelengths and group delays of the MRRs

<table>
<tr><th rowspan="2">Length of SMF (km)</th><th rowspan="2">Bandwidth (GHz)</th><th colspan="8">MRR No.</th></tr>
<tr><th>1</th><th>2</th><th>3</th><th>4</th><th>5</th><th>6</th><th>7</th><th>8</th></tr>
<tr><td>10</td><td rowspan="4">32</td><td>0
45.96</td><td>0.059
30.37</td><td>0.131
24.64</td><td>0.225
20.96</td><td>/</td><td>/</td><td>/</td><td>/</td></tr>
<tr><td>20</td><td>0
75.28</td><td>0.037
50.09</td><td>0.082
40.97</td><td>0.137
34.85</td><td>0.209
29.43</td><td>/</td><td>/</td><td>/</td></tr>
<tr><td>30</td><td>0
103.55</td><td>0.024
68.43</td><td>0.052
56.70</td><td>0.085
49.65</td><td>0.123
44.01</td><td>0.169
38.82</td><td>0.227
33.66</td><td>/</td></tr>
<tr><td>40</td><td>0
143.87</td><td>0.018
96.61</td><td>0.039
81.52</td><td>0.064
72.47</td><td>0.092
65.31</td><td>0.124
58.67</td><td>0.163
51.85</td><td>0.213
44.22</td></tr>
<tr><td>20</td><td>50</td><td>0
97.94</td><td>0.029
66.76</td><td>0.062
56.47</td><td>0.100
50.26</td><td>0.143
45.31</td><td>0.193
40.71</td><td>0.252
35.99</td><td>0.328
30.72</td></tr>
</table>

Note: The numerical data in the upper row in each grid represent the relative resonant wavelengths of each MRR with a unit of nm while those in the lower row stand for the group delay at the resonant wavelength of each MRR with a unit of ps.

Supplementary Note 3: Calibration of the dispersion compensator

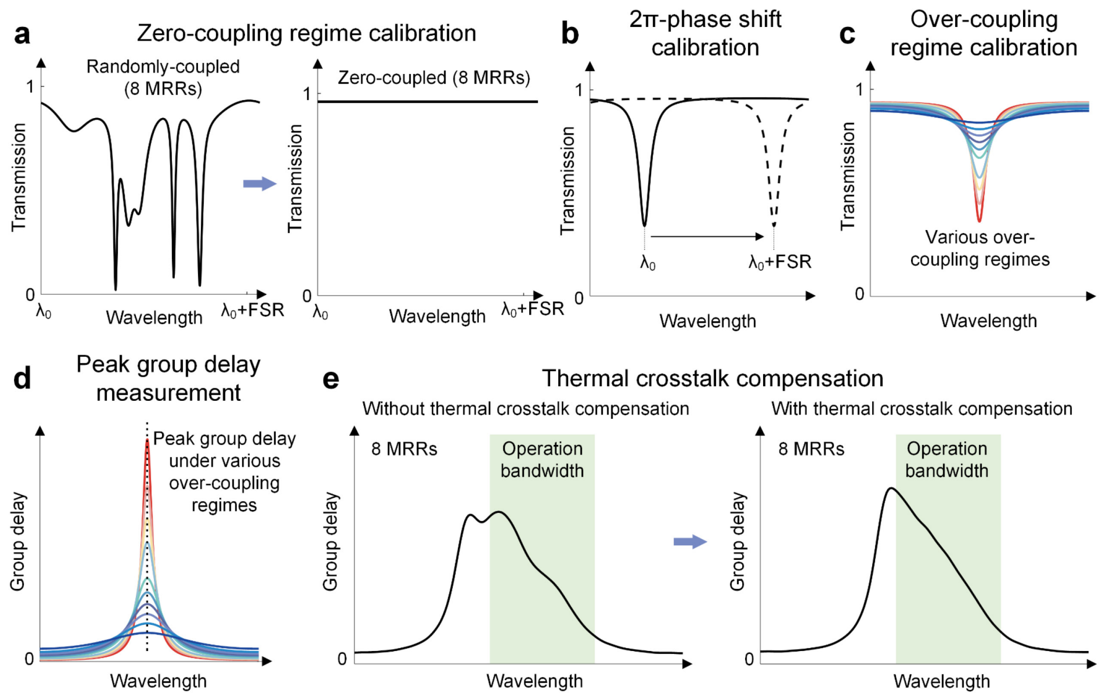

Supplementary Fig. 4. Schematics of the line shapes in various calibration steps. a Left: Schematics of the transmission under randomly coupled conditions for 8 MRRs. Right: Schematics of the transmission after zero-coupling regime calibration. **b** Schematics of the transmission of 2π-phase shift calibration. **c** Schematics of the transmission of over-coupling regime calibration. **d** Schematics of the group delay of the peak group delay measurement under various over-coupling regimes. **e** Left: Schematics of the group delay of 8 MRRs without thermal crosstalk compensation. Right: Schematics of the group delay of 8 MRRs with thermal crosstalk compensation.

Calibration of MRRs is essential in obtaining the best-performance dispersion compensator as all the MRRs are in coupling regimes and resonant wavelengths that generally deviate from their designed characteristics when no control voltages or algorithms are applied. As shown in Supplementary Fig. 4, we divide the calibration protocol into 5 steps: (1) the zero-coupling regime calibration of 8 MRRs (Supplementary Fig. 4a), (2) the 2π-phase shift calibration of the resonant wavelength of each MRR (Supplementary Fig. 4b), (3) the over-coupling regime voltage range calibration of each MRR (Supplementary Fig. 4c), (4) the group delay measurement under various over-coupling regimes of each MRR (Supplementary Fig. 4d), and (5) the thermal crosstalk compensation (TCC) of 8 MRRs (Supplementary Fig. 4e). We first implemented the zero-coupling calibration because in the following calibrations, we tuned the MRRs one by one, and we must tune all the other MRRs to the zero-coupling regime except for the one under tuning. Then, we calibrated the voltage for a 2π-phase shift of the resonant wavelength of each MRR to allow us to find the applied voltage needed for the resonant wavelength-tuning phase shifter of each MRR to tune the resonant wavelength. Next, as we tune each MRR according to the data shown in Supplementary Table 1, we need to obtain the group delay of each MRR under various over-coupling regimes. Finally, as we observed a severe thermal crosstalk-induced distortion of the measured responses after the (1) – (4) calibration steps, we further implemented the TCC to eliminate the influence of the thermal crosstalk. The detailed calibrations of each step are discussed in the following sections.

Firstly, each MRR was tuned to the zero-coupling regime by minimizing the resonant notches in the transmission spectrum to obtain the required voltage for the zero-coupling operation. Although the calibration objective is rather simple and clear, the transmission spectra of the zero- and unit-coupling regimes are almost identical except for the slightly different insertion losses, which makes it hard to distinguish between these two states by only referring to one flat transmission spectrum. As the resonant peaks are generally narrower and sharper in the under-coupling regime which is close to zero-coupling while they are wider and smoother in the over-coupling regime, we swept the applied voltage V_{i-cpl} $(1 \leq i \leq 8)$ on the phase shifter of the MRR coupler (the coupling-tuning phase shifter, as shown in Supplementary Fig. 2) one by one from 0 to 6 V with a step of 0.1 V, and measured the corresponding transmission spectra to identify the zero-coupling regime from the spectral lineshape. Supplementary Figures 5a and 5b show the normalized transmission spectra before and after the zero-coupling regime calibration. We obtained an insertion loss of ~6.2 dB, corresponding to an average insertion loss of 0.75 dB for each MRR. The first row of Supplementary Table 2 lists the required voltages for the zero-coupling regime of each MRR.

Supplementary Table 2. Configuration parameters of the MRRs

	Ring No.							
	1	2	3	4	5	6	7	8
Zero-coupling voltage (V)	5.150	6.225	6.050	6.050	6.050	5.725	6.150	6.050
2π-phase shift voltage (V)	5.575	5.750	5.800	5.750	5.750	5.600	5.875	5.775
Over-coupling voltage range (V)	3.4~4.4	2.9~4	2.7~4.1	2.9~4.2	2.9~4.2	2.5~4	2.9~4	2.9~4.3
FSR (nm)	0.807	0.807	0.806	0.807	0.807	0.807	0.806	0.806

Next, we calibrated the 2π-phase shift voltages of each MRR by increasing the voltage V_{res} on the phase shifter in the MRR (the resonant wavelength-tuning phase shifter, as shown in Supplementary Fig. 2) until the resonance shifts by one FSR. The other MRRs were tuned to the zero-coupling regime. The second row of Supplementary Table 2 shows the measured 2π-phase shift voltages for the 8 MRRs, which are in the range of 5.575 V to 5.875 V, corresponding to a power consumption varying from 17.27 mW to 19.18 mW.

After that, we swept the voltages on the coupling-tuning phase shifters to obtain the voltage ranges for the over-coupling regime. We identified the over-coupling regime by referring to the transmission spectrum of the critical-coupling regime, which exhibits a maximum extinction ratio (ER) among all the operational conditions. The third row of Supplementary Table 2 illustrates the voltage ranges of the over-coupling regime of each MRR. The FSR of each MRR is also shown in Supplementary Table 2. During all the calibration steps, a thermo-electric cooler (TEC) was placed under the dispersion compensator chip to control the on-chip temperature, which was set to 20℃.

Next, we measured the group delay responses under the over-coupling regime to obtain the relationship between the peak group delay and the applied coupling voltages of all the MRRs. We tuned the MRR under test to realize various coupling coefficients in the over-coupling regime while measuring the corresponding group delay responses. During this procedure, we tuned the MRR one by one and the other MRRs were tuned to the zero-coupling regime. Supplementary Figures 5c and 5d show the measured transmission and group delay responses of the first MRR under various power coupling coefficients in the over-coupling regime. In this test, we fixed the resonant

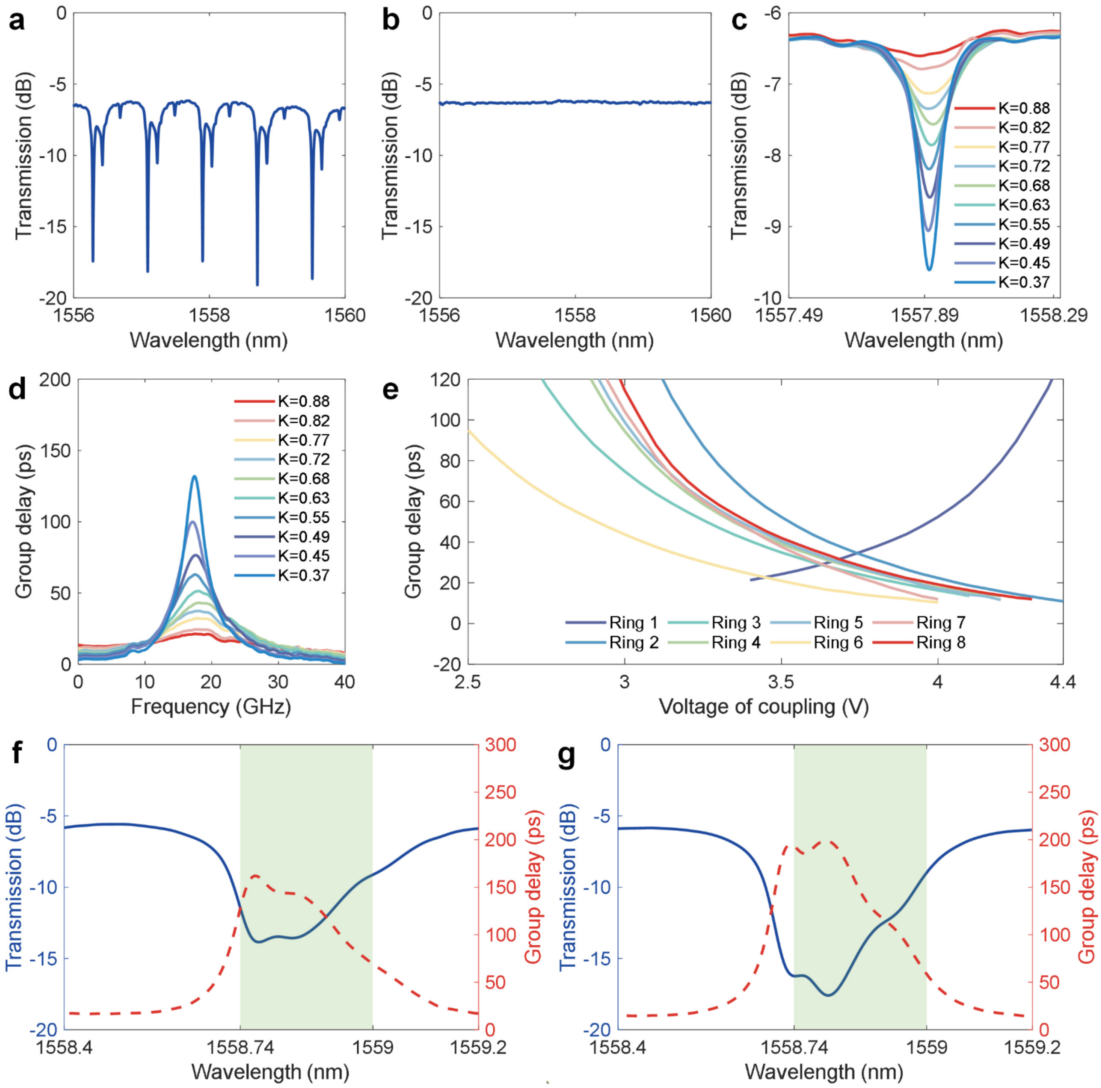

Supplementary Fig. 5. Experimental calibrations of the dispersion compensator. a, b Measured transmission spectrum **(a)** before and **(b)** after the zero-coupling regime calibration. **c, d** Measured **(c)** transmission spectra and **(d)** group delay responses of the first MRR with various power coupling coefficients under over-coupling regimes. **e** Measured maximum group delays with respect to the applied coupling voltages of 8 MRRs. **f, g** Measured transmission and group delay responses of dispersion compensation for **(f)** 30 km and **(g)** 40 km SMFs transmission without the TCC.

wavelengths of all the MRRs to the same wavelength by adjusting the resonant wavelength-tuning phase shifters upon varying the coupling coefficient. The extracted relationship between the peak group delay and the applied coupling voltage of each MRR is shown in Supplementary Fig. 5e. We attribute the different trend of the first MRR to the fabrication error-caused reverse coupling change of the MZI coupler. For the first MRR, K_{eqv_1} first increases with the increased θ_{1_1} (when the coupler voltage is under 3.4 V), and then decreases with the increased θ_{1_1} (when the coupler voltage is in the range of 3.4 V to 4.4 V), indicating that the initial phase difference of the MZI coupler is $\Delta\phi_{ini_1} < 0$. For the other MRRs, $\Delta\phi_{ini} > 0\ (i = 2, 3, \dots, 8)$. The fabrication error causes the opposite sign of the initial phase difference of the first MRR.

Following the calibration results, we can tune all the MRRs to achieve the dispersion compensation states for various lengths of SMFs. We fist extracted the peak group delay and the corresponding resonant wavelengths of each MRR from the simulation, as shown in Supplementary Table 1. Then, we acquired the required voltages for the coupling tuning from the measured relationship between the peak group delay and the applied voltages on the couplers, as shown in Supplementary Fig. 5e, and then we applied the voltages to the MRRs under test. Next, we adjusted the resonant wavelength from the initial wavelength to the desired one. We measured the transmission spectrum in the range of 1556 nm to 1560 nm to extract the resonant peak wavelength λ_{1_i}, and then we calculated an applied voltage on the resonant wavelength-tuning phase shifter by:

$$V_{i-res} = \sqrt{\frac{\lambda_{0_i} - \lambda_{1_i}}{FSR_i} \cdot V_{i_{2\pi}}^2} \tag{7}$$

where λ_{0_i}, FSR_i, and $V_{i_{2\pi}}$ denote the desired resonant wavelength in free space, the free spectral range, and the 2π-phase-shift voltage for the resonant wavelength tuning of the i$^{\text{th}}$ MRR. We implemented several iterations (no more than 3) in this wavelength-tuning process. We note that all the eight MRRs were tuned one by one. While one MRR was tuned, the other MRRs were adjusted to the zero-coupling state with no applied voltages to the resonant wavelength-tuning phase shifters. After completing the calibration of each MRR, we applied the acquired voltages to all the MRRs together to achieve the desired dispersion compensation. The measured transmission and group delay responses for dispersion compensation of 30- and 40-km-long SMFs are shown in Supplementary Figs. 5f and 5g, in which we noted a severe distortion. This distortion mainly originates from the thermal crosstalk (TC) between MRRs, which results in a severe degradation of the signal quality. Therefore, the TCC is essential to optimize the dispersion compensator.

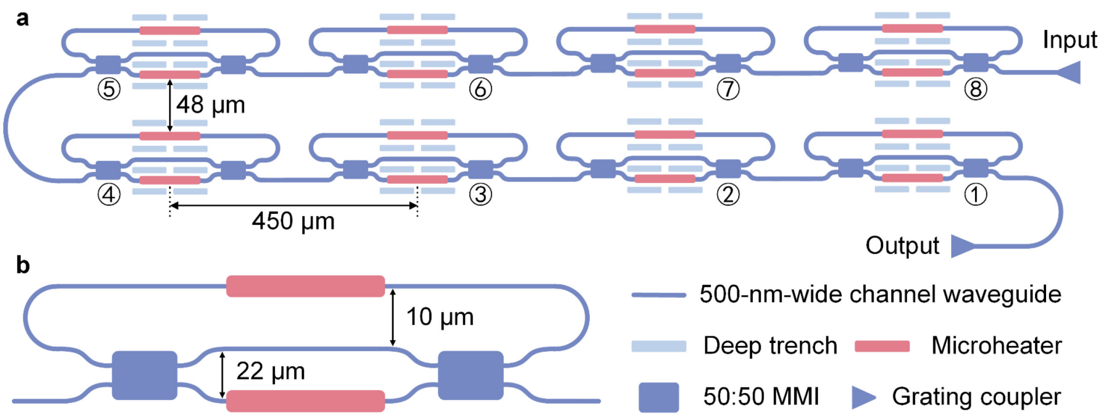

Supplementary Fig. 6. Schematic of the dispersion compensator. a Schematic layout of the 8 MRRs. The numbers label the sequence of MRRs. **b** Schematics of one MRR. Deep trenches are removed for a clear indication of the distance between waveguides. MMI: multimode interferometer.

Supplementary Figure 6a shows the schematic layout of the dispersion compensator. The distances between the adjacent MRRs in the row and column directions are 450 μm and 48 μm, respectively. One MRR is shown in Supplementary Fig. 6b with the deep trenches removed for a better indication of the distances between the waveguides. The two arms of the MZI are separated by 22 μm, and the upper arm is 10-μm away from the straight waveguide in the MRR. There are mainly two types of TCs in the layout of the 8 MRRs. One is the intra-TC, which originates from the two phase shifters inside one MRR, and the other is the inter-TC, which comes from the TC between the MRRs.

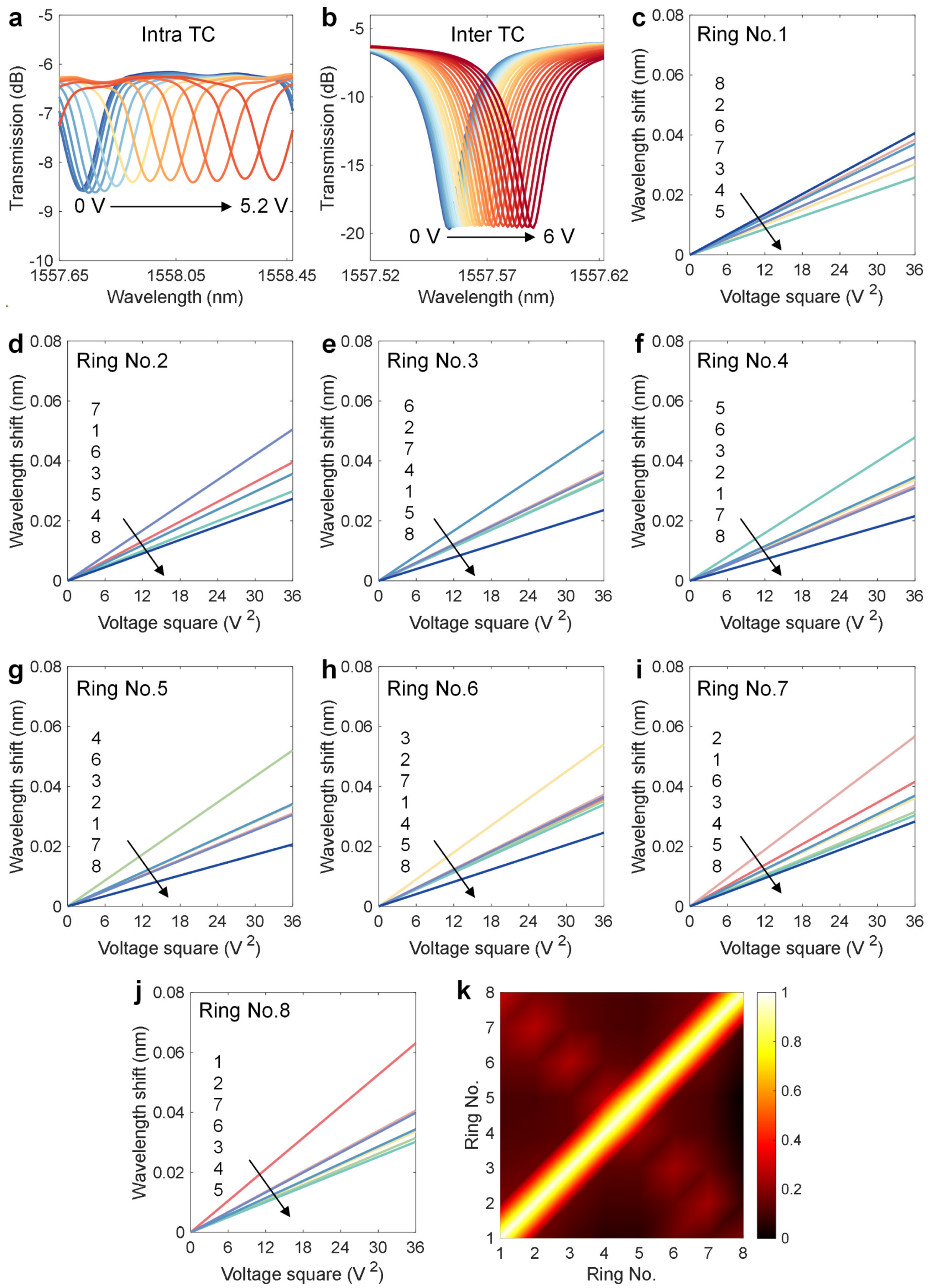

Supplementary Fig. 7. Characterizations of intra- and inter-TC of the dispersion compensator. a Measured transmission spectra of the first MRR when the wavelength-tuning phase shifter is applied with voltages. **b** Measured transmission spectra of the third MRR when the wavelength-tuning phase shifter of the second MRR is applied with voltages. **c-j** Measured resonant wavelength shift of the **(c)** first, **(d)** second, **(e)** third, **(f)** fourth, **(g)** fifth, **(h)** sixth, **(i)** seventh, and **(j)** eighth MRR when the resonant wavelength-tuning phase shifters of the other MRRs (indicated by labeled numbers) are applied with voltages. The MRR with the number on the top has the severest inter-TC to the MRR under test. **k** Normalized thermal crosstalk matrix of 8 MRRs.

For the intra-TC, as the MZI coupler is a part of the MRR, the coupling tuning in one arm of the MZI coupler intrinsically shifts the resonant wavelength. We calibrated this resonant wavelength shift during the over-coupling calibration process as the resonant wavelengths are fixed at the same wavelengths under the over-coupling regime. Therefore, the intra-TC mainly indicates whether the coupling is influenced by the tuning of the resonant wavelength of the same MRR. As all the MRRs share the same design, we chose one of them for the analysis. Supplementary Figure 7a shows the measured transmission spectra of the first MRR with V_{1-res} swept from 0 V to 5.2 V with a step of 0.4 V. We tuned the MRR to the over-coupling regime and observed no evident coupling deviation, indicating that the intra-TC from the resonance tuning is negligible. As a result, we ignore the thermal influence of other MRRs on the coupling of the MRR under test as the phase shifters of the other MRRs are located even further away.

Therefore, we only need to consider the influence of inter-TC to the resonant wavelength shift of one MRR when tuning the resonant wavelengths and the coupling coefficients of all the other MRRs. Supplementary Figure 7b shows the measured transmission spectra of the third MRR when V_{2-res} was swept from 0 V to 6 V with a step of 0.2 V. The resonant wavelength red-shifts with an increased V_{2-res}. Although a wavelength shift of only 0.04 nm was observed under a 6-V applied voltage, this inter-TC must be carefully considered because the overall performance of our dispersion compensator is sensitive to the resonant wavelength of each MRR. Therefore, we swept $V_{i-res}\,(i = 1, 2, \dots, 8)$ one by one, and obtained the corresponding transmission spectra. Supplementary Figures 7c to 7j show the linearly fitted wavelength shift of the i^{th} MRR when $V_{j-res}\,(j = 1, 2, \dots, 8,\ j \neq i)$ changes from 0 to 6 V. Here we take the first MRR for example. The impact of the inter-TC is sorted as 8>2>6>7>3>4>5, meaning that the 8^{th} MRR has the most severe inter-TC to the 1^{st} MRR and the 5^{th} MRR has the mildest impact. To precisely characterize the influence of inter-TC, we extracted the slope of each line and obtained a thermal crosstalk matrix (TCM) as follows:

$$\mathrm{T} = 10^{-2} \cdot \begin{pmatrix} 2.5600 & 0.1070 & 0.0841 & 0.0718 & 0.0716 & 0.1030 & 0.0908 & 0.1130 \\ 0.1100 & 2.4200 & 0.0988 & 0.0830 & 0.0831 & 0.0993 & 0.1400 & 0.0760 \\ 0.0948 & 0.1020 & 2.4000 & 0.0954 & 0.0942 & 0.1390 & 0.1010 & 0.0655 \\ 0.0869 & 0.0885 & 0.0938 & 2.4200 & 0.1330 & 0.0962 & 0.0861 & 0.0599 \\ 0.0861 & 0.0862 & 0.0939 & 0.1450 & 2.3900 & 0.0949 & 0.0848 & 0.0574 \\ 0.0998 & 0.1030 & 0.1500 & 0.0977 & 0.0943 & 2.5500 & 0.1020 & 0.0683 \\ 0.1150 & 0.1580 & 0.1000 & 0.0876 & 0.0844 & 0.1030 & 2.3500 & 0.0786 \\ 0.1750 & 0.1130 & 0.0935 & 0.0874 & 0.0839 & 0.0955 & 0.1110 & 2.3900 \end{pmatrix} \qquad (8)$$

All the elements of the TCM have a unit of nm/V^2, meaning that the resonant wavelength of the i^{th} MRR red-shifts T_{ij}-nm when 1 V is applied on the j^{th} MRR, where T_{ij} represents the matrix element on the i^{th} row and the j^{th} column. The diagonal matrix elements represent the resonant wavelength tuning efficiency of the i^{th} MRR while the other elements are the inter-TC efficiencies. The normalized TCM is graphically shown in Supplementary Fig. 7k. The different levels of inter-TC demonstrate that the TC is the most severe between the MRRs located in the same column while it reduces when the MRRs are separated far away in the layout. We can readily understand this phenomenon as the micro-heater tends to heat up more along the longer side than along the shorter side, and the heat diffuses with length. We characterized the impact of the inter-TC when the couplings of other MRRs were tuned and found that it is almost identical to the one caused by the wavelength tuning, which we attribute to the close placement of the coupling-tuning and the wavelength-tuning phase shifters. Therefore, we can utilize the obtained TCM for the compensation of the inter-TC induced by the coupling tuning.

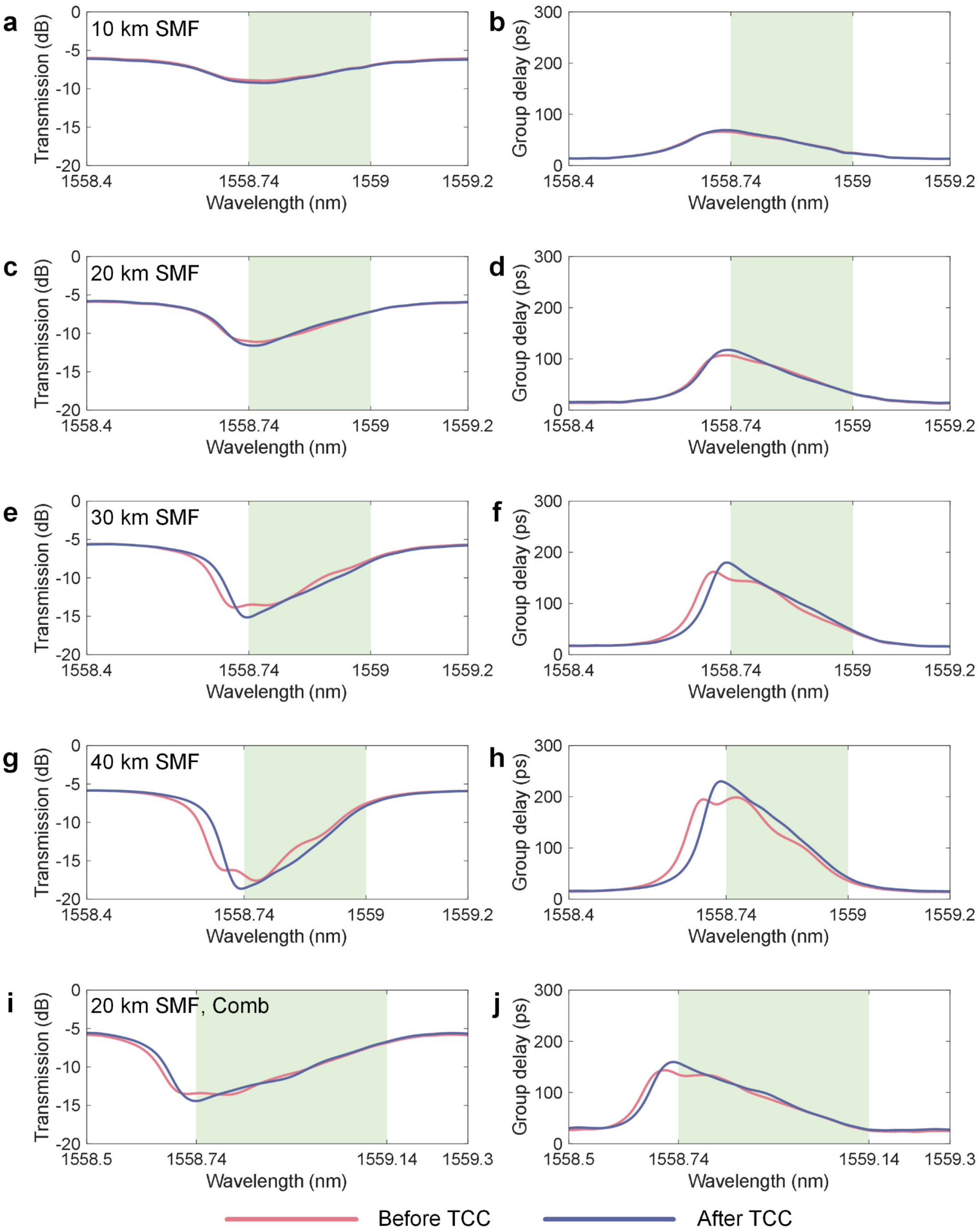

Supplementary Fig. 8. Measured transmission and group delay responses before and after the TCC. a-h Measured transmission spectra and group delay responses of dispersion compensation within 32-GHz bandwidth for **(a, b)** 10 km, **(c, d)** 20 km, **(e, f)** 30 km, and **(g, h)** 40 km SMFs transmission before and after the TCC. **i, j** Measured **(i)** transmission spectra and **(j)** group delay responses of dispersion compensation within 50-GHz bandwidth for 20-km SMF transmission before and after the TCC.

Finally, with the obtained TCM, we can compensate for the TC-induced wavelength shift and obtain the correct dispersion compensation state. As the TC has a negligible influence on the coupling coefficient of the MRRs, the applied voltages for the coupling tuning V_{i-cpl} $(i = 1, 2, \ldots, 8)$ are directly obtained according to the data shown in Supplementary Fig. 5e. To compensate for the influence of the inter-TC, we modify the applied voltage to the resonant wavelength-tuning phase shifter of the i^{th} MRR as:

$$V_{i-final} = \sqrt{V_{i-res}^2 - \sum_{1\le j\le 8, i\ne j}\left(\frac{T_{ij}V_{j-res}^2}{FSR_i}\cdot V_{i_{2\pi}}^2\right) - \sum_{1\le j\le 8, i\ne j}\left(\frac{T_{ij}\left(V_{j_{DC}}^2 - V_{j_{ZC}}^2\right)}{FSR_i}\cdot V_{i_{2\pi}}^2\right)} \quad (9)$$

where $V_{i_{2\pi}}$ is the 2π-phase shift voltage of the i^{th} MRR, and $V_{j_{ZC}}$ and $V_{j_{DC}}$ represent the applied voltages of the zero-coupling regime and of the desired-coupling regime of the j^{th} MRR, respectively. The applied voltages before and after the TCC are demonstrated in Supplementary Table 4. The power consumption is less than 160 mW.

Supplementary Table 4. Applied voltages before and after the TCC

		Length of SMF (km)	MRR No.							
			1	2	3	4	5	6	7	8
Coupling-tuning voltage (V)		10	3.925	3.825	3.725	3.900	6.050	5.725	6.150	6.050
		20	4.200	3.525	3.375	3.575	3.700	5.725	6.150	6.050
		30	4.325	3.350	3.175	3.350	3.450	3.075	3.550	6.050
		40	4.400	3.200	2.950	3.125	3.200	2.800	3.350	3.450
		20 (Comb)	4.300	3.350	3.175	3.325	3.425	3.050	3.525	3.700
Wavelength-tuning voltage (V)	Before the TCC	10	4.823	5.360	3.716	3.803	0	0	0	0
		20	4.698	5.420	3.672	3.529	4.958	0	0	0
		30	4.636	5.443	3.574	3.363	4.699	4.841	2.807	0
		40	4.608	5.475	3.595	3.346	4.683	4.715	2.493	4.790
		20 (Comb)	4.666	5.435	3.653	3.452	4.834	4.800	3.039	5.953
	After the TCC	10	4.858	5.365	3.662	3.771	0	0	0	0
		20	4.760	5.441	3.635	3.501	5.015	0	0	0
		30	4.809	5.581	3.675	3.470	4.847	4.997	2.881	0
		40	4.834	5.659	3.764	3.516	4.875	4.915	2.654	4.920
		20 (Comb)	4.751	5.525	3.699	3.496	4.941	4.906	3.024	6.013

The transmission and the group delay responses before and after the TCC for the dispersion compensation for the 10-, 20-, 30-, and 40-km-long SMFs in a 32-GHz bandwidth and for the 20-km-long SMF in a 50-GHz bandwidth are illustrated in Supplementary Figs. 8a to 8j. Compared with the results without the TCC, the transmission and the group delay responses show much less distortion and exhibit a superior linearity within the operation bandwidth after the TCC. The impact of the TC is larger for the dispersion compensation with more utilized MRRs, which is because more TC is introduced with more utilized MRRs. We note that although some other TCC approaches based on thermal eigenmode decomposition have been proposed in the literature[3, 4], iterations are required to evaluate the exact elements of the TCC matrix. However, no iterations are required based on our TCC method, which simplifies calibration of the MRR-based dispersion compensators. This method is applicable for other integrated photonic circuits based on thermal phase tuning. All the calibration tests were accomplished by software in our experiments.

Supplementary Note 4: 64-Gbit/s PAM4 data transmission using a CW-laser

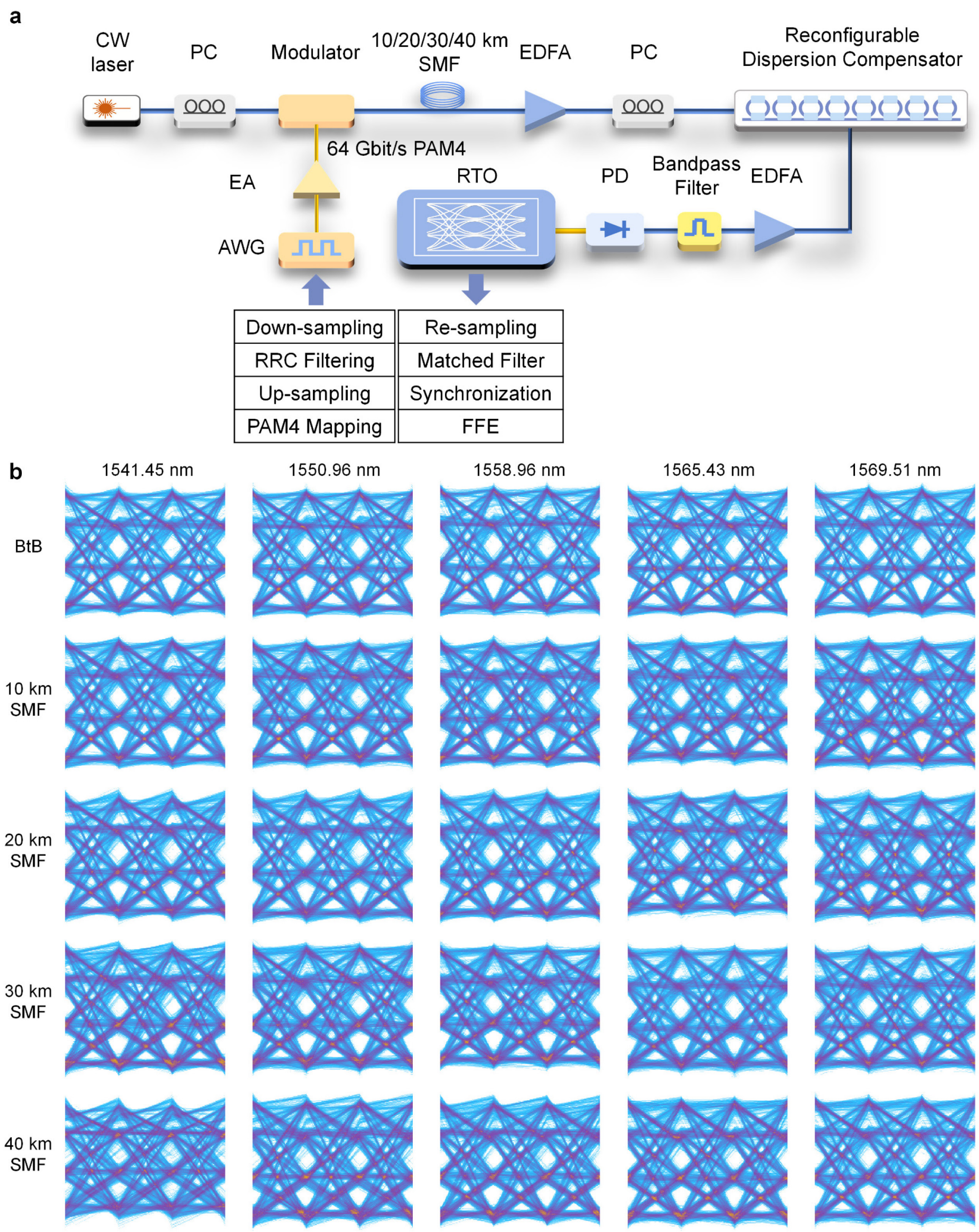

Supplementary Fig. 9. CW-laser-based data transmission. a Experimental setup schematics of signal transmission for dispersion compensation for 10-, 20-, 30-, and 40-km-long SMFs using a CW laser as the light source. CW: continuous-wave; PC: polarization controller; EDFA: erbium-doped fiber amplifier; EA: electrical amplifier; AWG: arbitrary waveform generator; PD: photodetector; RTO: real-time oscilloscope; RRC: root-raised cosine; FFE: feed-forward equalization. **b** Eye diagrams for BtB and transmissions with dispersion compensation under various wavelengths and lengths of SMFs.

The experimental setup schematics of the signal transmissions with dispersion compensation for 10-, 20-, 30-, and 40-km-long SMFs in a 32-GHz bandwidth under 5 different wavelengths in the C-band is shown in Supplementary Fig. 9a. The wavelengths of 1541.45 nm, 1550.96 nm, 1558.96

nm, 1565.43 nm, and of 1569.51 nm were chosen in the experiment. All the wavelengths were arbitrarily chosen except for 1558.96 nm, at which the dispersion compensator was calibrated. The output power from the continuous-wave (CW) laser was maintained at 12.5 dBm for all the measurements. A pulse-amplitude four-level modulation (PAM4) signal generated by an arbitrary waveform generator (AWG, Keysight 8199A) with a maximum sampling rate of 256 GSa/s was amplified by an electrical amplifier and then applied to drive a 40-GHz-bandwidth commercial intensity modulator (iXblue MXAN-LN-40). After the transmission over the lengths of the SMFs, we amplified the modulated signal by an erbium-doped fiber amplifier (EDFA) to ensure that the power of the optical signal after the dispersion compensator was kept at about -5 dBm, which is intended to compensate for the non-uniform loss across a broad wavelength span introduced by the grating coupler. We utilized another EDFA to ensure the power of the received optical signal at the 50-GHz photodetector (PD, Finisar XPDV2320R) was maintained at around 3 dBm. We obtained the electrical waveforms using a real-time oscilloscope (RTO, Keysight Z592A) with a sampling rate of 80 GSa/s for offline digital signal processing (DSP).

The measured eye diagrams of the data transmission under back-to-back (BtB) conditions, and the transmissions with dispersion compensation for the 4 different lengths of the SMFs in a 32-GHz bandwidth under the 5 wavelengths are shown in Supplementary Fig. 9b. The eye diagrams are clear with open eyes in the BtB transmissions, and we obtained comparable ones after the dispersion compensation. The eye diagrams without dispersion compensation are shown in Fig. 2e in the manuscript. They are blurred with closed eyes without dispersion compensation.

Supplementary Note 5: 80-Gbit/s PAM4-based parallel data transmission

The experimental setup schematics of the microcomb-driven parallel PAM4 data transmission is shown in Fig. 3a of the manuscript. In the experiment, the 7th channel of the comb lines (1558.96 nm) was aligned with the center of the operation bandwidth of the dispersion compensator. We show the measured eye diagrams of all the 15 comb lines in the BtB and the dispersion-compensated transmissions in Supplementary Figs. 10a and 10b. Compared with the other eye diagrams, those of the 1st, 13th,14th, and 15th channels were slightly distorted owing to the FSR mismatch between the comb lines and the dispersion compensator.

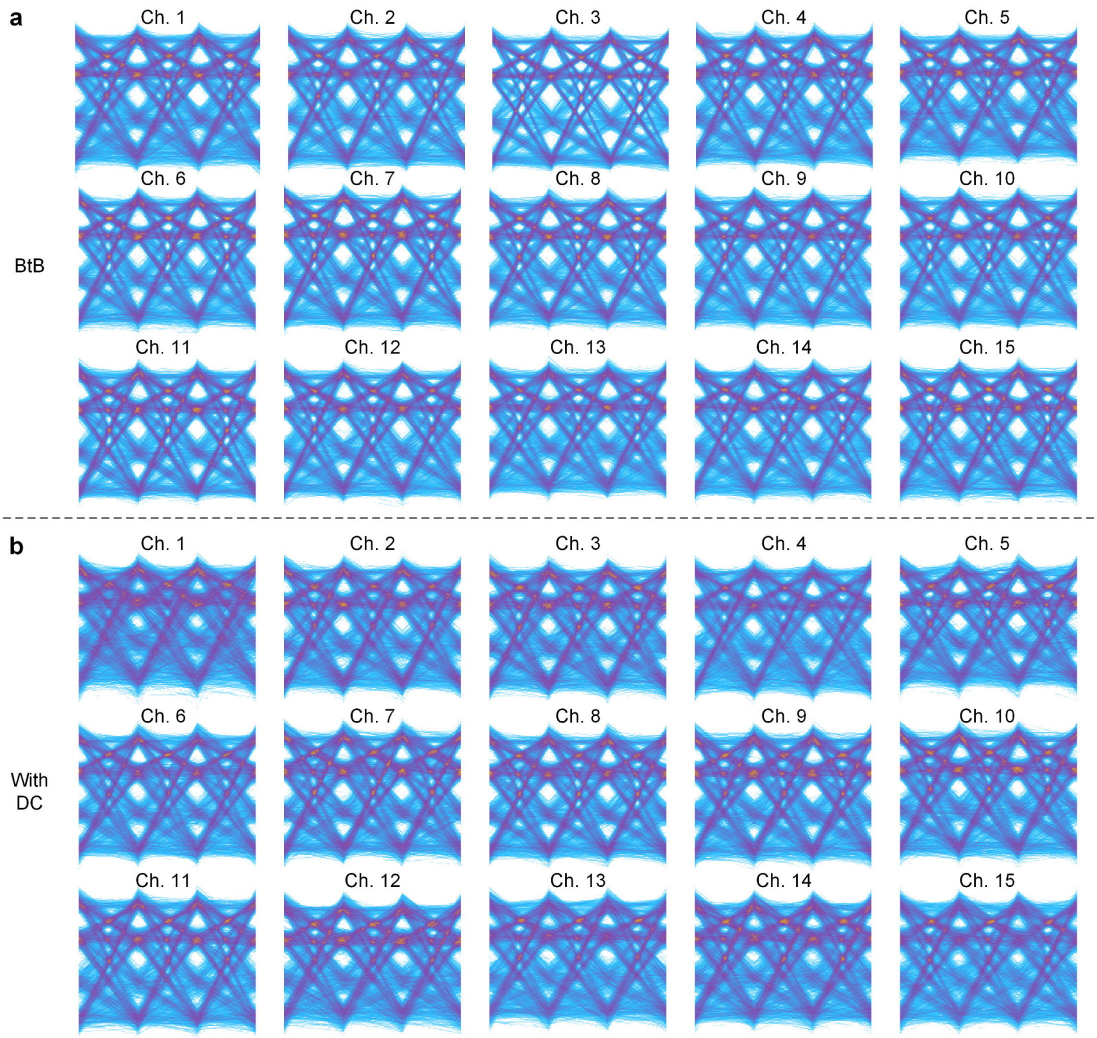

Supplementary Fig. 10. Microcomb-based 80-Gbit/s PAM4 parallel data transmission. a, b Eye diagrams of 15 comb lines using 80-Gbit/s PAM4 modulation signal under **(a)** BtB transmission and **(b)** transmissions with dispersion compensation. DC: dispersion compensation.

Supplementary Note 6: 112-Gbit/s DMT-based parallel data transmission

The experimental setup schematics of the 112-Gbit/s DMT-based parallel data transmission is shown in Extended Data Fig. 1 in the manuscript, which is almost identical to that of the PAM4-based parallel data transmission except for the DSP procedures and for the modulation format. During the measurement, we obtained the constellations of the total 160 sub-carriers of each comb line, and those of the 7th sub-carrier, with a 16-QAM modulation format, of all the 15 comb lines after dispersion compensation are shown in Supplementary Fig. 11. The constellations are only slightly deteriorated after the fiber transmission, indicating an excellent dispersion compensation performance of our device.

As for the bit rate of the DMT transmission, we calculate the raw bit rate by 64 GSa/s×297bits/(2×80GSa/s+10) = 112 Gbit/s, where 64 GSa/s and 80 GSa/s are the sampling rates of the AWG and of the RTO, 297 is the total number of bits of one DMT symbol, and 10 is the length of the cyclic prefix sequence. We transmitted a 112 Gbit/s DMT signal in each channel of the 15 comb lines, which leads to an aggregate total bit rate of 15*112 Gbit/s = 1.68 Tbit/s.

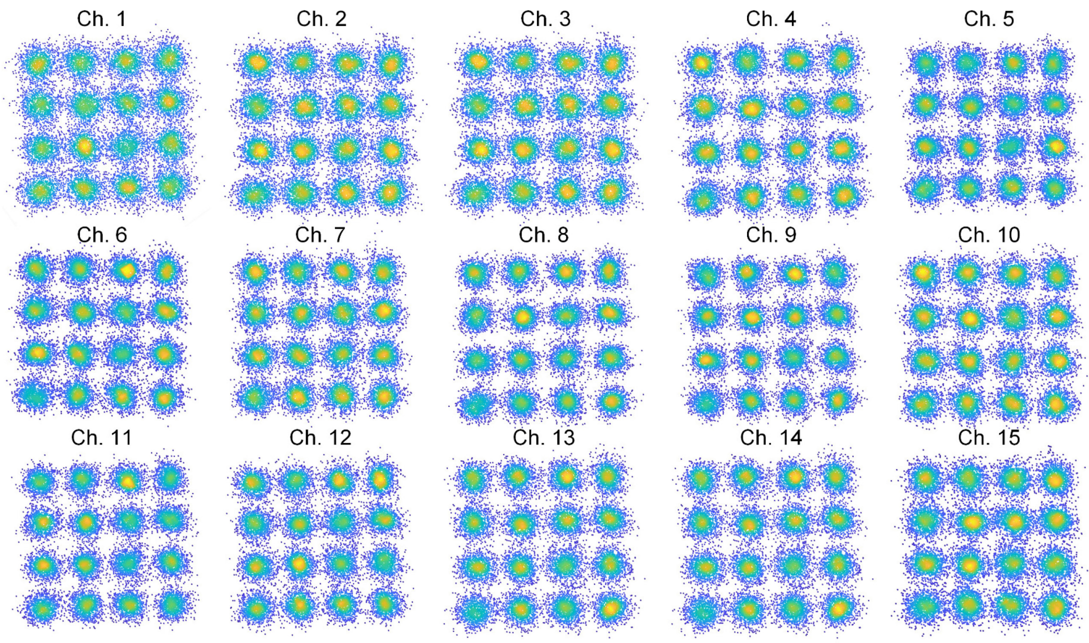

Supplementary Fig. 11. Microcomb-based 112-Gbit/s DMT parallel data transmission. Constellations for 16-QAM modulation of the 15 comb lines using a 112-Gbit/s DMT signal after the dispersion compensation for the 7th sub-carrier.

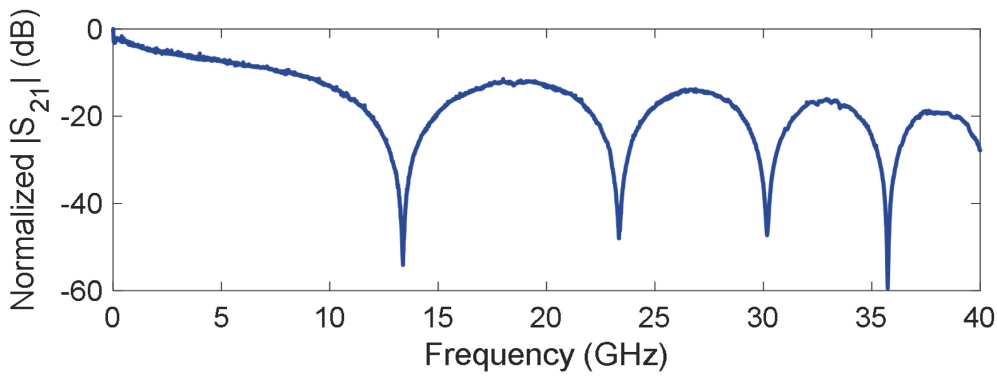

Supplementary Fig. 12. Measured normalized S_{21} magnitude response of the 20-km SMF. The FSF-induced response null points appear at the frequencies of around 13 GHz, 23 GHz, 30 GHz, and 36 GHz.

Supplementary Figure 12 shows the measured S_{21} magnitude response of the 20-km SMF in a frequency span of less than 40 GHz. The dispersion-induced frequency-selective fading (FSF) leads to periodic null points at the frequencies of around 13 GHz, 23 GHz, 30 GHz, and 36 GHz, which accounts for the measured high bit-error rates (BERs) at the frequencies of 13 GHz and of 23 GHz without dispersion compensation in the experiments shown in Fig. 4d of the manuscript.

References

1. Zhang HY, Lu LJ, Chen JP, Zhou LJ. Program-Controlled Single Soliton Generation Driven by the Thermal-Compensated Avoided Mode Crossing. *Journal of Lightwave Technology* **41**, 1801-1810 (2023).
2. Fujii S, Tanabe T. Dispersion engineering and measurement of whispering gallery mode microresonator for Kerr frequency comb generation. *Nanophotonics* **9**, 1087-1104 (2020).
3. Milanizadeh M, Aguiar D, Melloni A, Morichetti F. Canceling Thermal Cross-Talk Effects in Photonic Integrated Circuits. *Journal of Lightwave Technology* **37**, 1325-1332 (2019).
4. Milanizadeh M*, et al.* Control and Calibration Recipes for Photonic Integrated Circuits. *IEEE Journal of Selected Topics in Quantum Electronics* **26**, 1-10 (2020).